Competition between the bulk and the dissociation layer in electrohydrodynamic flow of dielectric liquid around coplanar electrodes

Y. K. Suh and K. H. Baek

Department of Mechanical Engineering, Dong-A University, 840 Hadan-dong, Saha-gu, Busan 604-714, Korea

(Received 28 August 2012; revised manuscript received 4 October 2012; published 13 February 2013)

An experimental and numerical study has been conducted on the electrohydrodynamic flow around coplanar electrodes with a dielectric liquid: dodecane mixed with the surfactant Span 80. It is shown that the flow is asymmetric, although the electrode is symmetrically arranged, and numerically, we have shown that a difference in the ionic size can reproduce such asymmetric patterns. It is also found that the dissociation layer effect becomes more important in determining the flow pattern than is predicted from the conventional theory where the Langevin formula is used for the recombination constant. In numerical simulations, reducing the recombination constant to 0.035–0.055 times the Langevin value turned out to produce good comparisons between the experimental and the numerical results for the electrode pairs with 1 and 0.2 mm gaps.

DOI: 10.1103/PhysRevE.87.023009 PACS number(s): 47.65.−d, 47.61.−k

I. INTRODUCTION

The dielectric liquid is characterized by very low electric permittivity and a very low concentration of free ions. Therefore, it has been frequently used as an insulating material in engineering applications, e.g., electric power transformers and electrophoretic image displays (see Ref. [1] for the relevant literature). Long exposure of the dielectric liquid to the environment, however, causes unavoidable entrainment of moisture and impurities, which, subjected to a high electric field, can transform to free ions and can cause charge accumulation and electrical breakdown. Therefore, understanding the creation of charge, ion transport, and fluid flow of a dielectric liquid is important for the optimum design and operation of such electrical devices.

When an electric field is applied across a pair of electrodes submerged in a dielectric liquid, free ions are created from the impurities (ion dissociation), and simultaneously, the free cations and anions combine to become neutral ion pairs (recombination). In the bulk, the ion dissociation is in equilibrium with the ion recombination, and so the bulk remains almost at a neutral state. Separately, the rate of ion dissociation has been found to increase with the applied electric field intensity, which is called the Onsager effect. Therefore, we can expect a nonuniform distribution of ion concentrations and, subsequently, a nonzero conductivity gradient even in the bulk. As is shown later, when the conductivity gradient is not orthogonal to the electric field, charge is created. Together with the charge injection from electrodes, it is the main cause of the electrohydrodynamic (EHD) flow of dielectric liquids under a high electric field. On the other hand, within the thin dissociation layers (to be referred to as DSL hereafter) near the electrodes, the ion dissociation dominates the ion recombination, and counterion concentration is higher than the coion concentration. Therefore, the DSL is thin, but the level of charge is much higher than the bulk.

There is a strikingly different aspect of EHD flow generation between the bulk space charge and the DSL charge. The former drives the fluid flow spontaneously because the body force is spread over the whole domain, whereas, the latter drives the flow with a time lag because the body force is confined to thin layers on the electrode surfaces.

There have been few papers on the flow of a dielectric liquid created by the Onsager effect in the bulk. Ryu *et al.* [2] conducted experimental studies on the EHD flow around circular conducting cylinders and over a nonconducting sphere subjected to a uniform external ac electric field. More recently, Kim *et al.* [3] studied the realization of the Onsager effect in fluid pumping with three cylindrical electrodes. They attributed the observed fluid flow to the nonzero space charge density caused by the Onsager effect in the bulk. In their papers, however, the effect of the DSL was neglected.

The primary object of this paper is to demonstrate that the flow driven by the DSL becomes more important than that by the bulk as the geometric scale is decreased. In addition, we show that reproduction of the experimental data can be accomplished by significantly reducing the recombination constant.

II. GOVERNING EQUATIONS AND NUMERICAL METHODS

A. Full equations for two-dimensional simulation

We consider a dielectric liquid of density ρ and viscosity η confined within a square cavity of side length L as shown in Fig. 1. A pair of electrodes is located at $y = 0$, the bottom of the cavity, with the gap distance d. We take $L = 16d$ large enough that the EHD flow around the gap becomes as free as possible from the sidewall effect.

Governing equations for the steady-state incompressible fluid flow driven by the Coulomb force, acting on ion concentrations, can be written in terms of the fluid velocity $\mathbf{u}$ and the pressure p as follows:

$$\nabla \cdot \mathbf{u} = 0, \tag{1a}$$

$$\rho\,(\mathbf{u}\cdot\nabla)\,\mathbf{u} = -\nabla p + \eta\nabla^2\mathbf{u} + \rho_q\mathbf{E}, \tag{1b}$$

where $\rho_q = e(z_1c_1 + z_2c_2)$ is the space charge density, e is the elementary charge, c_1 and c_2 are concentrations of the cation and anion, respectively, and z_i is the valence; we consider monovalent ions and take $z_1 = 1$ and $z_2 = -1$. Furthermore, $\mathbf{E} = -\nabla V$ is the electric field, and V is the electric potential.

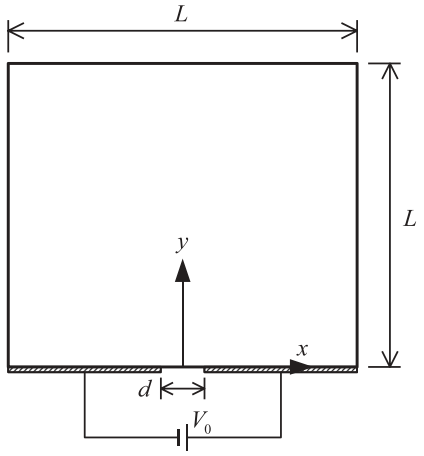

FIG. 1. Computational domain with a pair of coplanar electrodes on the bottom wall subjected to a dc voltage difference V_0.

The potential is given by solving the Poisson equation,

$$\varepsilon_0\varepsilon_r\nabla^2 V = -\rho_q, \tag{2}$$

where ε_0 and ε_r are the vacuum permittivity and the relative permittivity of the fluid, respectively. In this paper, we determine the charge density by solving the full steady-state transport equations for binary ions of unit valence. The concentration of ion i, c_i, is described by the transport equation,

$$\mathbf{u}\cdot\nabla c_i + \nabla\cdot(-D_i\nabla c_i + z_i\mu_i\mathbf{E}c_i) = R_i. \tag{3}$$

Here, $D_i = k_BT/(6\pi\eta a_i)$ is the diffusivity, $\mu_i = e/(6\pi\eta a_i)$ is the mobility, a_i is the ionic radius, k_B is the Boltzmann constant, and T is the temperature. The right-hand-side (RHS) term of Eq. (3) reading

$$R_i = \alpha\left[c_0^2F_O(b) - c_1c_2\right] \tag{4}$$

denotes the source of ion concentrations [1]. The first term corresponds to the rate of ion dissociation, and the second corresponds to the rate of recombination where c_0 is the zero-field concentration. The function,

$$F_O(b) = I_1(2b)/b \tag{5}$$

represents the Onsager effect. I_1 is the modified Bessel function of the first kind of order 1, $b = 2\sqrt{\gamma E}$ is a function of the field intensity $E = |\mathbf{E}|$, and

$$\gamma = e^3/\left(16\pi\varepsilon_0\varepsilon_r k_B^2T^2\right) \tag{6}$$

is the Onsager constant [1]. The recombination constant α in Eq. (4) is to be obtained from Langevin's formula [4],

$$\alpha_L = \frac{e(\mu_1+\mu_2)}{\varepsilon_0\varepsilon_r}. \tag{7}$$

However, in order to match the experimental results, in this paper, we propose to reduce this constant with the reduction factor κ; $\alpha = \kappa\alpha_L$. A more detailed discussion on the Langevin formula is given in Sec. IV. Later in this paper, we see that a significant reduction in the recombination constant is required to obtain successful agreement between the experimental and the numerical results in both qualitative and quantitative respects. For later use, we derive the order of the DSL thickness from the balance between the conduction term $\nabla\cdot(z_i\mu_i\mathbf{E}c_i)$ and the ion dissociation term $\alpha c_0^2F_O(b)$ in Eq. (3) as follows:

$$\delta_{\mathrm{DSL}} = \frac{\varepsilon_0\varepsilon_r E_\infty}{2\kappa e c_0}, \tag{8}$$

where E_∞ is the electric field evaluated at the edge of the DSL. In deriving (8), we set $z_i = 1$, $\mu_i = (\mu_1+\mu_2)/2$, $c_i = c_0$, and $F_O = 1$.

Boundary conditions for the above system of equations are as follows: $\mathbf{u} = 0$ all over the surrounding boundaries, $c_2 = V = 0$ on the cathode [left-hand side (LHS) electrode], $c_1 = 0$ and $V = V_0$ on the anode (RHS electrode), and zero charge ($\partial V/\partial n = 0$) and no ion flux ($\partial c_i/\partial n = 0$) over the other walls, where n denotes the coordinate normal to the wall.

B. Simplified approximate equations for the bulk

Subtracting Eq. (3) for $i = 2$ from that for $i = 1$ yields

$$\nabla\cdot(\sigma\nabla V) = 0, \tag{9}$$

or $\nabla\cdot\mathbf{i} = 0$, where $\mathbf{i} = \sigma\mathbf{E}$ is the current density vector. Here,

$$\sigma = e(\mu_1c_1 + \mu_2c_2) \tag{10}$$

is the conductivity. From Eqs. (9) and (2), we can also derive the formula for the space charge density,

$$\rho_q = -\varepsilon_0\varepsilon_r\nabla(\ln\ \sigma)\cdot\mathbf{E}. \tag{11}$$

Note that Eqs. (9) and (11) are valid everywhere in the domain including the DSLs. However, within the DSL, distributions of c_1 and c_2 are not available without solving the ion transport equations (3), implying that Eq. (9) is not helpful if the DSLs are not excluded from the solution domain.

Now, we derive approximate but useful equations under the assumption of negligible DSLs. For the bulk, we can assume ion neutralization and equilibrium between the ion dissociation and recombination, i.e., $R_i = 0$, from which we can write

$$c_1 = c_2 = c_0\sqrt{F_O(b)}, \tag{12}$$

$$\sigma = 2e\bar{\mu}\,c_0\sqrt{F_O(b)}, \tag{13}$$

where $\bar{\mu} \equiv (\mu_1+\mu_2)/2$ is the algebraic mean of the mobilities. Note that these are again functions of the field intensity E because the Onsager function $F_O(b) = 1 + 2\gamma E + O[(\gamma E)^2]$ increases with E. Now Eq. (9) together with Eq. (13) can be solved for the potential V with the boundary conditions for V set the same as before. If E is small enough such that $\gamma E \ll 1$, Eq. (11) reduces to

$$\rho_q = -\varepsilon_0\varepsilon_r\gamma\nabla E\cdot\mathbf{E}. \tag{14}$$

This indicates that, when the electric field intensity increases along the electric field direction, negative space charge density is created and vice versa. In the neighborhood of the edge of the anode, the direction of $\mathbf{E}$ opposes that of ∇E, so we can expect positive charge density. Similarly, near the cathode edge, we expect negative charge density.

C. Numerical methods

We have solved the above system of equations by using the commercial software COMSOL (version 4.3). A preliminary

TABLE I. Radius of free ions in nonpolar liquids reported in the literature.

Solvent	Surfactant	Ionic radius (nm)	Source
Dodecane	AOT	1.5	Hsu *et al.* [5]
Dodecane	AOT	1.6	Roberts *et al.* [6]
Dodecane	AOT	1.5	Kemp *et al.* [7]
Dodecane	Span 80	2.25	Abou-Nemeh and Bart [8]
Hexane	Span 85	1.4	Guo *et al.* [9]
Kerosene	Span 80	14.6, 0.5	Dukhin and Goetz [10]

calculation, however, revealed that the magnitude of the ion-concentration difference $c_1 - c_2$ is much smaller than that of c_1 or c_2 itself over the whole domain, except in the thin DSLs; typically, $|c_1 - c_2|/c_1 \sim 10^{-5}$. Thus, distribution of the numerically given space-charge density ρ_q shows a significant number of wiggles, in particular, near the electrode edges. To partly overcome this, we introduce perturbed variables f_i defined as $c_i = c_0\sqrt{F_O(b)} + f_i$; f_i tends to vanish in the bulk thanks to (12). We substitute this into Eq. (3) and move all the terms to the RHS, except those which follow the standard form of the transport equation (3) specified by COMSOL. The RHS terms derived in this way serve as modified sources to the transport equations for f_i.

Since thin DSLs are expected to exist near the electrodes, fine structured boundary-layer grids are constructed near the electrodes. Using formula (8), we can predict the thickness of the DSL for $\kappa = 1$ in the range from 0.05 μm at the corners, $x = \pm L/2$, to 1 μm at the electrode edges, $x = \pm d/2$, where E_∞ is approximated as $E_\infty = V_0/(\pi x)$. After several test runs, we set the smallest grid size Δy on the electrode walls at 1 nm. In addition, we need to build clustered triangular grids around the electrode edges to resolve the steep gradient of the variables there. Test runs indicate that the maximum element size of the free triangles in controlling the clustering around the edges should be set less than 20 μm.

Aside from the two-dimensional (2D) numerical simulation, we also performed a one-dimensional (1D) simulation on the DSL near the electrode under the assumption that the tangential derivatives of variables are negligible compared with the normal derivatives. A detailed description of the numerical methods is given in Ref. [1]. The 1D simulation is useful, for example, in checking the validity of the boundary-layer grids built near the electrodes for the DSLs.

D. Parameter setting

There are several parameters involved in the above set of equations to be specified for numerical simulation. We fix $T = 295$ K, $\varepsilon_r = 2$, and $\eta = 1.34 \times 10^{-3}$ Pa s. In order to determine the mobilities, we use the Einstein equation $\mu = e/(6\pi\eta a)$, and thus, we must know the ionic radius. Table I lists the ionic radii of some of the nonpolar liquids reported in the literature. Since we use dodecane as the solvent and Span 80 as the surfactant mixture, we choose 2.25 nm as the averaged ionic radius following Abou-Nemeh and Bart [8]. Since we know the averaged ionic radius, we can calculate the averaged mobility from the Einstein relation. However, even though the mobility ratio $m = \mu_2/\mu_1$ is specified, mobility of each ion takes a different value depending on how the averaged mobility is defined. When the algebraic mean of the mobility $\bar{\mu}$ is used, we can get each mobility by using $\mu_1 = 2\bar{\mu}/(1+m)$ and $\mu_2 = m\mu_1$. However, the Einstein equation shows that each of the mobilities is in a reciprocal relation with the corresponding ionic radius. So, the Einstein equation, in its original form, cannot be directly used in calculating $\bar{\mu}$ from the algebraic mean of the ionic radius $\bar{a} \equiv (a_1 + a_2)/2$. On the other hand, when the geometric mean $\hat{\mu} \equiv \sqrt{\mu_1\mu_2}$ is used, the Einstein equation allows us to evaluate it directly from the geometric mean of the ionic radius $\hat{a} \equiv \sqrt{a_1 a_2}$ because they are in a reciprocal relation. To summarize, for a given mean radius $\hat{a}$ and mobility ratio m, we get $\hat{\mu}$ by using the Einstein equation and get each mobility from $\mu_1 = \hat{\mu}/\sqrt{m}$ and $\mu_2 = \hat{\mu}\sqrt{m}$. Then, the zero-field concentration c_0 is determined from the zero-field conductivity $\sigma_0 = 2e\bar{\mu}c_0$, which is to be taken from the first experiment as explained in the following section.

III. EXPERIMENTAL METHODS

We prepared nonpolar liquid dodecane (No. 297879, Sigma-Aldrich). We mixed the surfactant Span 80 (No. 85548, Sigma-Aldrich), to enhance the EHD flow following the reasons explained in Refs. [10,11], with 0.5 wt % fraction. Two kinds of experiments are performed with this liquid.

In the first experiment, the current-voltage curve is obtained from a pair of facing circular disk electrodes (1.5 mm thick) made from stainless steel; the diameter of the disks is 52 mm, and the gap spacing is 3.7 mm. We set a ring-shaped acryl spacer, similar to the one in Ref. [11] with an inner diameter of 50 mm between the disks in order to avoid the singular distribution of the field near the electrode edges. Applying a dc voltage V_0 across the electrodes by using a power-supply amplifier (Model 610E, Trek, Inc.), we measure the current by using a multimeter (Model 2000, Keithley Instruments, Inc.). The data set (E, i), obtained in this way, is fitted with the nonlinear i-E curve $i = \sigma E$ where the conductivity σ is given from Eq. (13). In this formulation, we have two unknown parameters, i.e., the zero-field concentration c_0 and the algebraic mean of the mobility $\bar{\mu}$, but fortunately, these two are combined to appear in multiplication form. Thus, we can find the zero-field conductivity $\sigma_0 = 2e\bar{\mu}c_0$, which is determined in such a way that the i-E curve best fits the experimentally measured data. Later, in 2D simulation, when $\bar{\mu}$ is given, we can get c_0. The degree of fitting of the theory to the experiment is measured by the root-mean-square (rms) error with the i-E curve.

In the second experiment, we visualize EHD flows above the coplanar electrodes within a cavity. The indium tin oxide glass is etched to yield a pair of electrodes having a given gap spacing. In this experiment, we set the gaps at $d = 1$ and 0.2 mm. For both gaps, we build a three-dimensional glass cavity with a side length of $L = 10$ mm above the electrodes and fill the liquid to the full depth. Applying voltage differences $V_0 = 1000$ and 200 V between the electrodes for $d = 1$ and 0.2 mm, respectively, we capture the trajectories of particles mixed in the fluid by using a high-speed CCD camera (Model GX1050, Allied Vision Technologies, Inc.). Nylon particles (Model 10456, Kanomax, Inc.) with diameters of 4.1 μm and specific gravities of 1.02 are used for scattering laser light, shed

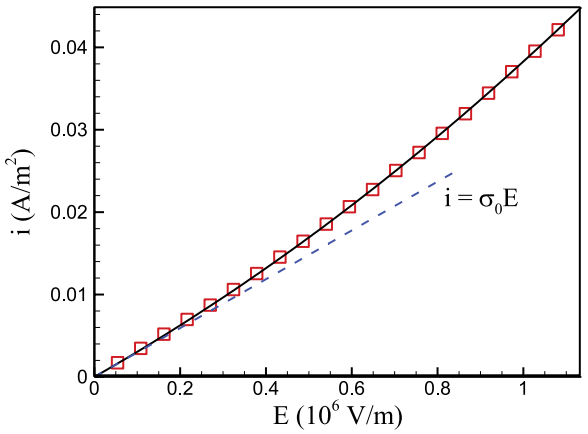

FIG. 2. (Color online) Symbols: experimentally measured data set (E, i) for dodecane mixed with 0.5 wt % Span 80, solid line: fitting by the nonlinear relation $i = \sigma E$ with the conductivity σ increasing with the field E following the Onsager theory. The dashed line represents Ohm's law with the zero-field conductivity $\sigma_0 = 2.96 \times 10^{-8}$ S/m.

on the midplane of the cavity in a sheet form. The recorded images are then used in performing streamlines and obtaining the 1D fluid-velocity distributions on the horizontal lines $y = 1$ and 0.4 mm for $d = 1$ and 0.2 mm, respectively.

In the flow-visualization experiment, we recorded images for more than 10 s and paid attention to using images taken after the flow was presumed to arrive at a steady state. On the other hand, long-time exposure of the fluid mixture to the electric field causes the particles to adhere to the electrodes. Order-of-magnitude analysis of the ion-transport equations indicates that the time scale for the ion migration reads $t_s \sim d/(\mu E) = 0.3$ s with the typical values of the mobility $\mu = 10^{-9}\text{m}^2\,\text{s}^{-1}\,\text{V}^{-1}$, the gap $d = 1$ mm, and the field intensity $E = 1$ kV/mm. The time scale for the fluid particle's advection can be derived as $t_s \sim d/u = 1$ s from the Navier-Stokes equations and typical flow velocity $u = 1$ mm/s. So, in principle, the images captured, at least, 4 s after switching on the voltage are expected to represent the steady-state flow. However, at smaller gaps, we had to wait for a longer time, until the flow showed a steady state.

IV. RESULTS AND DISCUSSIONS

From the i-E curve taken from the first experiment, we can get σ_0. It was found that the best fit to the experimental data with the Onsager constant $\gamma = 2.78 \times 10^{-7}$ m/V, given from Eq. (6), provides $\sigma_0 = 2.96 \times 10^{-8}$ S/m; see Fig. 2. We also computed the rms error with modified γ. It was found that $\gamma = 2.62 \times 10^{-7}$ m/V results in the best fit. However, this is only 6% smaller than the Onsager original constant. Considering the unknown experimental measurement errors, in this paper, we do not consider modification of γ from the Onsager theory. Thus, our measurement lends further support to the validity of the Onsager theory on the enhancement of dissociation with the increase in the field as also shown in Refs. [11,12]. Since $\hat{a} = 2.25$ nm was chosen, we get $\hat{\mu} = 2.82 \times 10^{-9}$ m^2 s^{-1} V^{-1}. Values of μ_1 and μ_2 are dependent on m. As a reference value, we get $c_0 = 3.28 \times 10^{19}$ m^{-3} for $m = 1$.

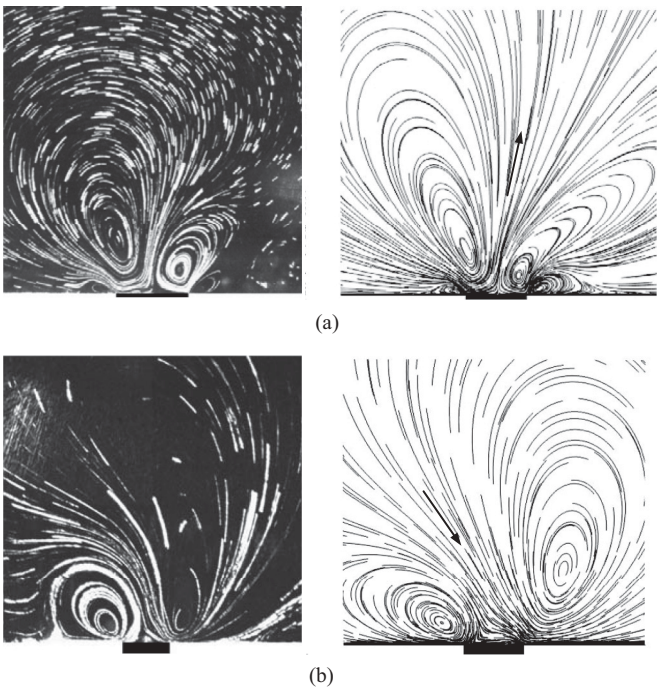

FIG. 3. LHS: visualized and RHS: numerical streamlines obtained for (a) $d = 1$ mm, $V_0 = 1$ kV and (b) $d = 0.2$ mm, $V_0 = 250$ V. Experimental results are taken 4 s later in (a) and 37 s later in (b) after the start. The numerical results are obtained with (a) $\kappa = 0.055$, $m = 0.75$, and (b) $\kappa = 0.035$, $m = 0.6$.

Figure 3 shows streamlines obtained from the experimental visualization and numerical simulations for two gap spacings. For the case with $d = 1$ mm [Fig. 3(a)], the flow pattern is initially almost symmetric, but it becomes asymmetric after a few seconds and remains at a steady state later on. The experimental streamline pattern of Fig. 3(a) is obtained with the images taken after 4 s from the start. A pair of large primary vortices (to be referred to as the "bulk vortex" hereafter) makes the fluid rise near the vertical central line $x = 0$ as indicated by an arrow in the numerical streamlines, and after turning around, it returns back to the gap region from both sides. Bulk vortices are, of course, created by the Coulomb force, originating from the nonzero space charge density in the bulk. As explained in Sec. II B with Eq. (14), we expect positive charge density near the RHS electrode edge and negative charge density near the LHS. Then, the Coulombic body force $\rho_q \mathbf{E}$ in the momentum equation (1b) is directed from the electrode edges to the central line $x = 0$ following the lines parallel to $\mathbf{E}$. This force should push the fluid upward, causing it to rise along the central line producing the bulk vortices.

On the other hand, two small vortices near the edges (to be referred to as the "DSL vortex" hereafter), seen in Fig. 3(a), are created by the Coulomb force in the thin DSLs near the electrode walls. Electrodes attract the counterions and repel the coions, leading to the emergence of highly concentrated positive charge density in the DSL of the cathode (LHS) and negative charge density in the DSL of the anode (RHS). Since the field in the DSL is directed almost normal to the wall, each DSL must show the pressure buildup. Such pressure buildup is strongest near the electrode edges and decreases as one moves

away from the edges, causing the fluid to flow toward the corners of the cavity. Such flow motion is also driven directly from the tangential component of the Coulomb force. Within the DSL near the cathode, for instance, the accumulation of cations brings a positive charge density as explained above and simultaneously brings an increase in E, which then causes a sharp increase in potential. The potential rise should be highest at the electrode edge and should decrease as $|x|$ is increased. The Coulombic force, acting on the counterions (cations), is then directed toward the LHS corner again, and thus, it directly drags the fluid in the same direction. Similar reasoning can be given for the DSL in the anode to show that the fluid moves toward the RHS corner. Since the Coulombic force is confined within the thin DSL, the resultant flow can be classified as a "surface-driven" flow. In a sense, the flow created by the induced charge in the DSL is similar to the "electro-osmotic flow" found in the aqueous solutions [13–19]; the fundamental difference is that the diffuser layer of the electric double layer in the aqueous solution is an outcome of the balance between the conduction and the diffusion terms in the ion-transport equation (3), whereas, the DSL in the nonaqueous solution results from the balance between the conduction and the ion dissociation (or source) terms. Now, let us return to the DSL vortices of Fig. 3(a). Since the bulk vortex on the LHS is counterclockwise, the fluid flow along the LHS electrode wall is directed toward the edge contrary to the DSL-driven flow. Thus, we can expect vortical flows, at least, near the edges, corresponding to the DSL vortices because the DSL-driven flow velocity, being highest near the edges, rapidly decreases as $|x|$ is increased, whereas, the bulk-driven flow velocity changes gradually along the x direction on the electrode walls.

In Fig. 3(a), we also show numerical streamlines, which are in agreement with those in the experiments. Most importantly, the numerical results are obtained with $\kappa = 0.055$, corresponding to a significant reduction in the recombination constant from α_L of Eq. (7). Previous papers [12,20,21] also report that the recombination constant for a certain medium should be lower than the Langevin value with the reduction factors of 0.7–0.8. In the present numerical simulation for $d = 1$ mm, when κ is taken larger than the optimum value 0.055, the DSL vortices become smaller, and the flow velocity becomes larger than the experimental results as discussed below. More details on the reduction in the recombination constant are given later in this section.

In Fig. 3(a), the DSL vortex on the RHS looks larger than that on the LHS, implying that the DSL effect is larger on the anode than on the cathode. Numerically, this asymmetry can be reproduced by assigning the mobility ratio m smaller than 1; the numerical results shown in Fig. 3(a) are obtained with $m = 0.75$. From the 1D numerical simulation, it was found that smaller m brings increased charge density and increased electric field intensity within the DSL on the anode, whereas, those values within the DSL on the cathode are decreased. Therefore, the decreased mobility ratio means a stronger DSL-driven flow on the anode wall and a weaker DSL-driven flow on the cathode wall. The difference in the mobility means the difference in the ionic radius. Dukhin and Goetz [10] performed the conductivity and electroacoustic measurements to assert that free anions in kerosene mixed with Span 80 are much larger than the cations (nearly 30 times).

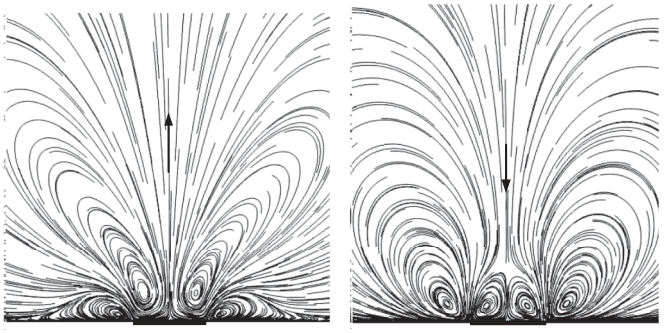

(a) (b)

FIG. 4. Streamlines obtained numerically for (a) $d = 1$ mm, $V_0 = 1$ kV and (b) $d = 0.5$ mm, $V_0 = 500$ V, showing flow reversal upon the variation in gap spacing; $\kappa = 0.045$ and $m = 1$.

The present matching for $d = 1$ mm predicts that the anion size is 1.33 times the cation size.

Figure 3(b) shows the streamline patterns for $d = 0.2$ mm where the experimental data are taken after 37 s from the start when a steady state is reached. At this gap, the flow pattern shows slow variation in time during the first tens of seconds. In this case too, we can observe two primary vortices on both sides of the central line $x = 0$. However, the fluid comes down between the two vortices as indicated in the numerical streamlines, and in fact, these vortices correspond to the DSL vortices. Such a dramatic difference in the flow direction between the large [Fig. 3(a)] and the small [Fig. 3(b)] gaps can be simply explained in terms of the competition between the bulk and the DSL effects; at $d = 1$ mm, the bulk effect is dominant, and so, the bulk vortices occupy the domain, whereas, at $d = 0.2$ mm, the DSL effect dominates over the bulk and determines the flow pattern in the reverse way.

The numerical streamlines in Fig. 3(b) are obtained with the parameter set $\kappa = 0.035$ and $m = 0.6$, which is taken different from that of $d = 1$ mm for the purpose of the best qualitative and quantitative matching between the numerical and the experimental results. The matching is satisfactory, except for a few aspects; for instance, the numerical DSL vortex on the LHS (to be referred to as the "D_L vortex") looks more slender than the corresponding experimental one, and the numerical D_R vortex looks fatter than the experimental one.

Qualitatively, we, thus, expect a transition of the bulk-dominant streamline pattern at large gaps to the DSL-dominant pattern at small gaps. We have numerically observed the transition with the parameters κ and m fixed at $\kappa = 0.045$ and $m = 1$ but with varying d. Figure 4(a) shows streamlines at $d = 1$ mm. The pattern is symmetric because we select $m = 1$, but otherwise, it looks similar to Fig. 3(a) as expected. The DSL vortices close to the bottom electrodes are somewhat larger than those of Fig. 3(a) because the value of $\kappa = 0.045$, used for Fig. 4(a), is smaller than that for Fig. 3(a). We, thus, characterize the flow as the bulk-dominant flow. As the gap is decreased, the DSL vortices grow, but the bulk vortices near the vertical centerline shrink, and at $d = 0.5$ mm, the bulk-dominant vortex structure is switched to the DSL-dominant flow [Fig. 4(b)]. As the gap is further decreased, the bulk vortices almost vanish, and only the DSL vortices occupy the domain as seen in Fig. 3(b).

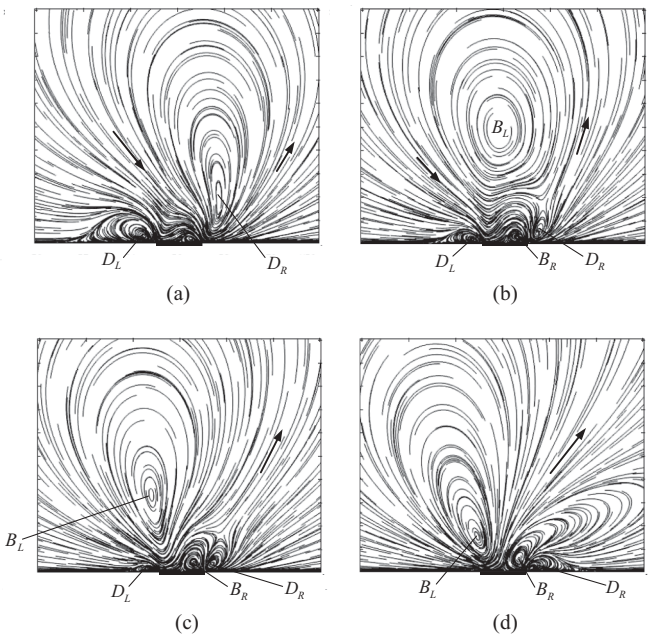

FIG. 5. Variation in the vortical flow pattern near the electrode gap upon the increase in κ with $m = 0.6$ for $d = 0.2$ mm; (a) $\kappa = 0.1$, (b) $\kappa = 0.15$, (c) $\kappa = 0.2$, and (d) $\kappa = 0.3$. The symbols B and D denote the bulk and the DSL vortices, respectively.

Such a transition is also observed at $d = 0.2$ mm with the variation in κ as shown in Fig. 5. This time, we set $m \neq 1$ and expect a more complex evolution of vortices. At $\kappa = 0.1$, the pattern [Fig. 5(a)] is qualitatively the same as that for $\kappa = 0.035$ shown in Fig. 3(b). At $\kappa = 0.15$, Fig. 5(b), the D_R vortex splits into B_L and D_R vortices due to the growing effect of the bulk. Later, the D_R vortex tends to reside near the edge of the RHS electrode. On the other hand, the B_R vortex, shrunk in the gap space at $\kappa = 0.1$, now grows to be comparable in size with the D_R vortex and later performs a pairing with it [Figs. 5(c) and 5(d)]. The D_L vortex, which, initially, was one of the primary ones, continues to become weakened and finally disappears at $\kappa = 0.3$ [Fig. 5(d)]. Overall, we observe the growth of bulk vortices and the decaying of DSL vortices with the increase in κ.

In Figs. 3(a) and 3(b), we can also see a difference between $d = 1$ and $d = 0.2$ mm in the inclination of the dividing streamline, which is defined as the streamline dividing the LHS and RHS vortices, i.e., roughly, the streamlines passing through the arrows in Fig. 3. In Fig. 3(a), the dividing streamline is inclined to the RHS, whereas, the one in Fig. 3(b) is inclined to the LHS, which is obviously a symptom of the asymmetric flow pattern. If the DSL effects on both sides are the same, then the fluid on the dividing streamline would go straightly vertical, but since the DSL effect on the RHS is stronger than that on the LHS, as occurs at m less than 1, the fluid motion must tend to shift to the RHS regardless of the flow direction.

Figures 6 and 7 show the measured and calculated distributions of the velocity components on the lines $y = 1$ and 0.4 mm for the gaps $d = 1$ and 0.2 mm, respectively. In the experimental measurement, for the gap spacing of 1 mm, 60 images recorded in the time interval 3.7 s $\leqslant t \leqslant$ 4.3 s are used, whereas, for the gap spacing of 0.2 mm, 200 images taken during 36 s $\leqslant t \leqslant$ 38 s are used in calculating the fluid velocity from the method of particle tracking; for the case of $d = 0.2$ mm, it took a longer time for the flow to arrive at the steady state because of unknown reasons. We can see that the experimental data are in satisfactory agreement with the numerical data obtained with reduced recombination constants. On the other hand, the numerical results, without a reduction in α, produce v_m, the local maximum of v near $x = 0$, too large (about seven times the experimental value; see Fig. 8) for $d = 1$ mm (Fig. 6) or even a difference in the sign of v_m for $d = 0.2$ mm (Fig. 7). This implies that, without a significant reduction in the recombination constant, we cannot numerically reproduce the experimental results both qualitatively and quantitatively.

Figure 8 shows the effect of κ on v_m numerically obtained at $m = 0.75$ and 0.6 for $d = 1$ and 0.2 mm, respectively. As far as the value of v_m is concerned, κ in the range of 0.04–0.05 should give the best matching, but for better matching in the streamline pattern, κ must have been taken larger for $d = 1$ mm and smaller for $d = 0.2$ mm than this range. For the case of $d = 0.2$ mm, we can see the change in sign in v_m near $\kappa = 0.2$ with an increase in κ, and we can now relate this to the shift from the downward to the upward fluid motion with

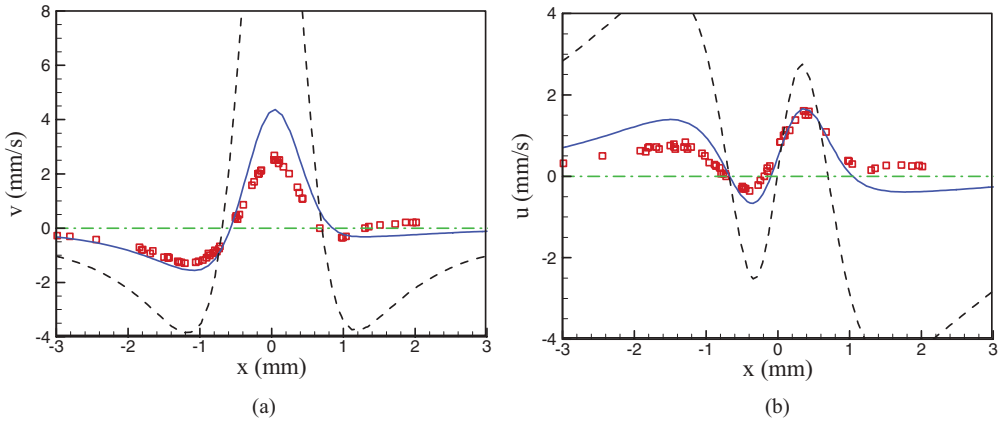

FIG. 6. (Color online) Distributions of (a) v and (b) u on $y = 1$ mm given from symbols: the experimental measurement and those given numerically at $m = 0.75$ with dashed line: $\kappa = 1$ and solid line: $\kappa = 0.055$ for $d = 1$ mm.

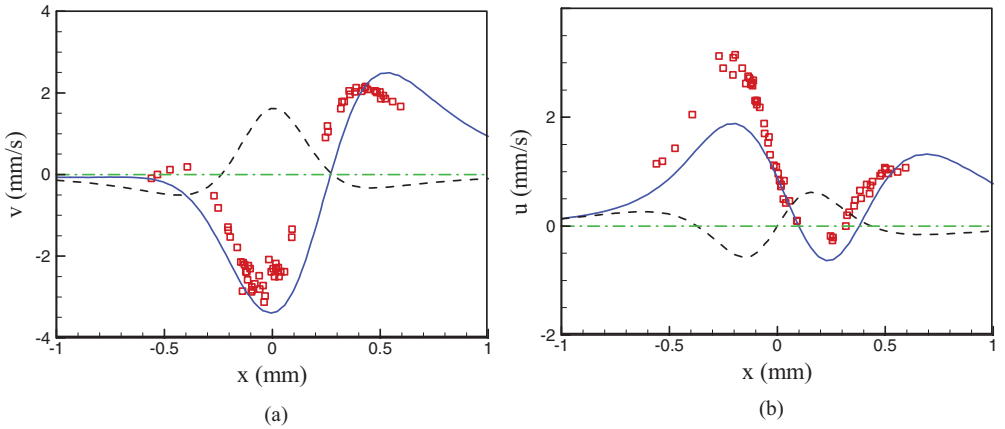

FIG. 7. (Color online) Distributions of (a) v and (b) u on $y = 0.4$ mm given from symbols: the experimental measurement and those given numerically at $m = 0.6$ with dashed line: $\kappa = 1$ and solid line: $\kappa = 0.035$ for $d = 0.2$ mm.

the increase in κ as explained above with Fig. 5. On the other hand, it should be noted that smaller values of κ tend to make the 2D simulation unstable.

The decrease in the mobility ratio $m \leqslant 1$ means more pronounced asymmetry. We performed 2D simulations with various values of m for $d = 0.2$ mm and $\kappa = 0.05$. It was found that, as m is decreased, the D_R vortex becomes bigger, and its center position moves upward, whereas, the D_R vortex becomes smaller, and its center position moves downward.

So far, we have seen that the recombination constant κ plays a determining role in the EHD flow. The decrease in κ is found to bring the increased effect of the DSL. In order to understand this, we perform a 1D simulation of the ion-transport problem for the DSL near the anode where $E_\infty = 0.398$ kV/mm is given from $E_\infty = V_0/(\pi x)$ with $V_0 = 250$ V and $x = 0.2$ mm. Figure 9 shows the numerical results obtained at three κ values. As κ is decreased, not only the field intensity, but also the layer thickness increase as can be seen from Eq. (8). From Eq. (8), we can estimate $\delta_{\mathrm{DSL}} \sim 15\ \mu$m for $\kappa = 0.05$ and $m = 1$ being consistent with Fig. 9. Integrating Eq. (2) over the DSL, we get

$$Q \equiv \int_0^\infty \rho_q dy = -\varepsilon_0 \varepsilon_r (E_w - E_\infty), \tag{15}$$

where E_w denotes the field values at the anode wall. This then indicates that the amount of charge in the DSL, Q, is proportional to the field rise $E_w - E_\infty$ within the DSL. Thus, a smaller κ causes a larger field rise, meaning a larger DSL charge and Coulomb force, which should give rise to the increased slip velocity at the edge of the DSL, leading to an increased DSL effect. Even for the same amount of Q, the difference in the pattern of the charge-density distribution can also affect the slip velocity. When the distribution is sharper, occurring, i.e., for a thinner DSL, the Coulomb force must

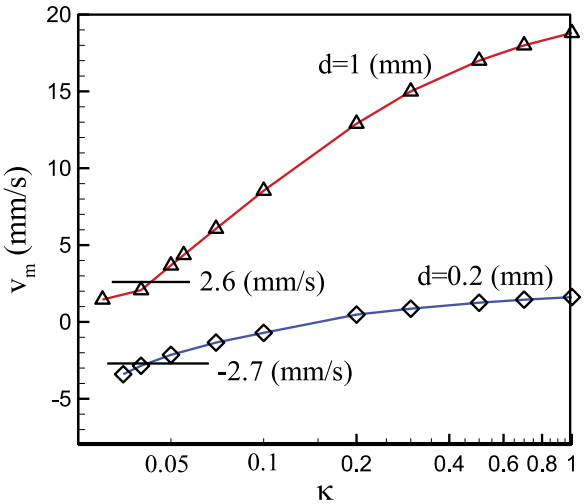

FIG. 8. (Color online) Effect of κ on v_m, the value of v at the point near $x = 0$ on the line $y = 1$ mm for $d = 1$ mm and that on $y = 0.4$ mm for $d = 0.2$ mm where the local maximum of $|v|$ occurs; data are obtained numerically with $m = 0.75$ for $d = 1$ mm and $m = 0.6$ for $d = 0.2$ mm. The horizontal lines indicate the experimentally measured values.

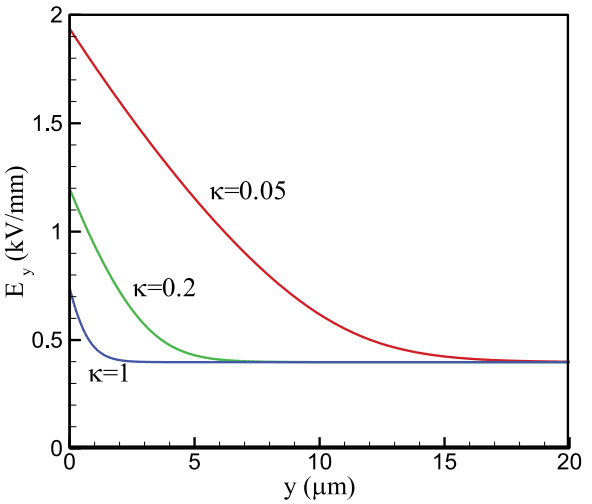

FIG. 9. (Color online) Effect of the recombination constant κ on the distribution of the field as a function of the distance measured from the anode obtained with a 1D numerical simulation for the external field $E_\infty = 0.398$ kV/mm (equivalently, a voltage difference of 250 V across the gap distance of 0.2 πmm) and the parameter set $\hat{a} = 2.25$ nm, $m = 0.6$, and $\sigma_0 = 2.96 \times 10^{-8}$ S/m.

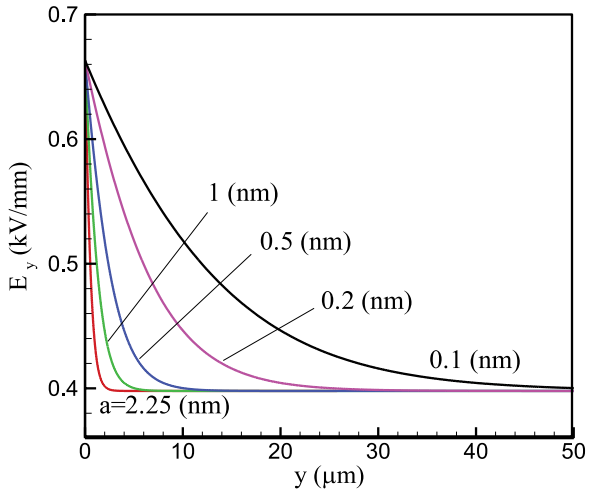

FIG. 10. (Color online) Effect of $\hat{a}$ on the field distribution within the DSL obtained with a 1D numerical simulation for the same external field as in Fig. 9 and the parameter set $\kappa = 1$, $m = 0.6$, and $\sigma_0 = 2.96 \times 10^{-8}$ S/m.

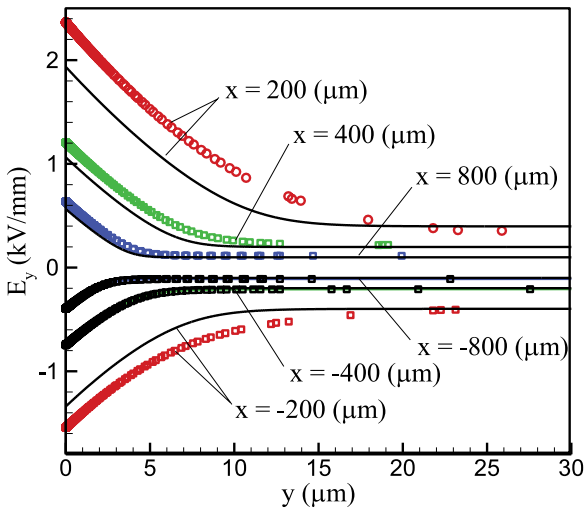

FIG. 11. (Color online) Distribution of the vertical component of the field E_y along the vertical lines at $x = \pm 0.2, \pm 0.4$, and ± 0.8 mm obtained from symbols: 2D and solid lines: 1D simulations for a 0.2 mm gap with $V_0 = 250$ V, $\kappa = 0.05$, and $m = 0.6$.

experience a larger friction force from the electrode wall than the case with a more gradual distribution with a thicker DSL, and so the slip velocity would decrease accordingly. This can be understood from double integration of the simplified 1D momentum equation $\eta\ \partial^2 u/\partial y^2 + \rho_q E_x = 0$ for the tangential velocity component, where E_x may be taken independent of y, for simplicity.

The above reasoning can be applied to the investigation of the effect of the ionic radius $\hat{a}$ on the field distribution within the DSL. Figure 10 shows 1D numerical results obtained for various $\hat{a}$'s with the gap $d = 0.2$ mm under the external field $E_y = 0.398$ kV/mm. Since the zero-field conductivity σ_0 is fixed, a decrease in the ionic radius means an increase in the mobility and a simultaneous decrease in the zero-field concentration, which creates an increase in the DSL thickness as can be seen from Eq. (8). This is also consistent with the numerical results given in Fig. 10. The numerical results also reveal that the field rise is not affected by the change in $\hat{a}$. So, the change in the ionic radius, if permitted, is not so effective in increasing the slip velocity compared with the change in the recombination constant. Furthermore, the range of the ionic size adjustment must be restricted because it can be measured more accurately with refined measurement tools.

In order to validate the 1D and 2D simulations, we compare the distribution of E_y, the vertical component of the field along the vertical lines attached on the electrode walls at several values of x, obtained from both methods as shown in Fig. 11. Obviously, better agreement is shown between the two results as $|x|$ is increased. As one approaches the electrode edges, the derivatives of variables with respect to x, which are neglected in the 1D simulation, become more important. We can also see that the anode side with $x > 0$ shows a thicker DSL than the cathode side with $x < 0$ because m is less than 1. Field rise is also larger on the anode side than on the cathode side, implying a larger slip velocity from the DSL on the anode side, being consistent with the discussions given so far.

Exploring the feasibility of adjusting the recombination constant in the numerical simulation for matching the experimentally measured flow data, we have found plausible evidence. Gäfvert *et al.* [22] managed to measure the electric field in a transformer oil confined within a pair of parallel electrodes receiving an external voltage 3.2 kV across the gap distance of 19 mm. With the zero-field conductivity known as $\sigma_0 = 10^{-11}$ S/m, we can control the mobility μ_1 (or the averaged ionic radius) to adjust c_0, whereas, the mobility ratio is fixed at $m = 2.1$. Figure 12 shows some of the 1D simulation results. When the recombination constant is fixed at Langevin's value, i.e., with $\kappa = 1$, the measured data cannot be reproduced by the 1D results with the tuning of μ_1. At very large μ_1 (or with a very small ionic radius), c_0 becomes very small, and the DSLs on both electrodes overlap each other, leading to a uniform distribution of the field (the line with

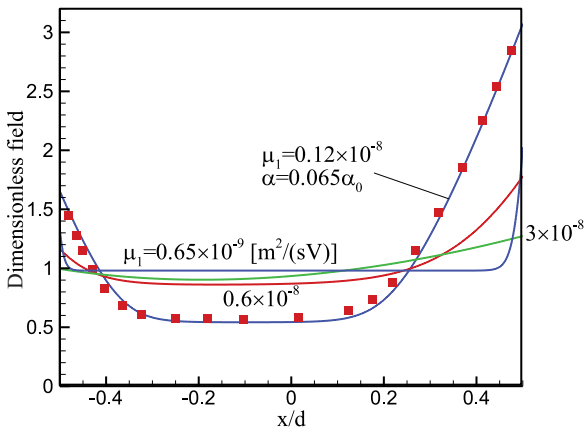

FIG. 12. (Color online) Distribution of the electric field in transformer oil confined between a pair of facing electrodes with the gap spacing of $d = 19$ mm, subjected to the external voltage difference of 3.2 kV. Symbols denote data measured by Gäfvert *et al.* [22]. The solid line near the symbols is given from the 1D simulation with $\mu_1 = 1.2 \times 10^{-9}$ m^2 s^{-1} V^{-1}, $\kappa = 0.065$ and $m = 2.1$. The other solid lines are given from the 1D simulation for several values of μ_1 at $\kappa = 1$ and $m = 2.1$.

$\mu_1 = 3 \times 10^{-8}$ m^2 s^{-1} V^{-1} in Fig. 12). On the other hand, when μ_1 is taken to be very small (or with a very large ionic radius), c_0 becomes very large, and the DSLs are very thin, corresponding to the line with $\mu_1 = 0.65 \times 10^{-9}$ m^2 s^{-1} V^{-1} in the figure. The intermediate value of μ_1 also cannot reproduce the measured field distribution. However, the data can be successfully matched when α is reduced down to 0.065 times the Langevin value at $\mu_1 = 0.12 \times 10^{-8}$ m^2 s^{-1} V^{-1}. With this mobility, the ionic radius is estimated to be 1 nm at $\eta = 7 \times 10^{-3}$ Pa s, which should not be far from the practical values for general nonpolar liquids, some of which are shown in Table I.

Formula (7) was derived by Langevin for ionic recombination in high-density gases, by Smoluchowski for neutral components, and by Debye [23] for more general cases; see, e.g., Ref. [4] for relevant references. In deriving (7), it is assumed that charge transport is purely diffusive. Suppose a negative charge is stagnant at a point (referred to as the reaction point) surrounded by a cloud of positive charges. When one of the surrounding positive charges is close enough to the central charge, say within the encounter distance r_c, the former is assumed to spontaneously collide with the latter, leading to neutralization. To compensate for the vacancy of the positive charge, the surrounding positive charges move (diffuse) toward the reaction point. On the other hand, for the system to be in a steady state, another negative charge is assumed to be created at the reaction point (e.g., via dissociation), and the process of neutralization is repeated in this way. The fundamental problem of determining the recombination constant in this situation is as follows: How many positively charged particles will collide per unit time with the negative charge? Smoluchowski stated that the problem can be solved by using a 1D steady diffusion equation for the concentration of positive charge under the boundary conditions with zero concentration at the encounter distance and a constant value far away. Then, we finally get

$$\alpha = 4\pi D r_c,$$

as the recombination constant, where $D = D_1 + D_2$. Choosing the encounter distance as $r_c = l_B$ and substituting the Einstein relation for the diffusivity, we arrive at the Langevin formula (7); here, $l_B = e^2/(4\pi\varepsilon_0\varepsilon_r k_B T)$ is known as the Bjerrum distance, obtained by equating the Coulomb potential and the thermal potential. Note that the Coulomb-force effect is not totally neglected, but it is considered in determining the encounter distance. Later, Debye [23] considered the Coulomb-force effect in addition to the diffusion and derived

$$\kappa = [1 - \exp(-l_B/r_c)]^{-1},$$

as the correction factor for the recombination constant, where r_c is now taken as $r_c = a_1 + a_2$. Note that $\kappa \to 1$ as $l_B/r_c \to \infty$, which is relevant for the liquid dielectric. So, for the liquid dielectric, the Langevin formula is still correct because the Coulomb effect has already been considered via the setting $r_c = l_B$. Collins and Kimball [24] proposed a modified model where it is assumed that not every countercharge particle, arriving at the encounter distance, necessarily reacts with the central charge. They introduced the so called "reaction parameter" k to show

$$\kappa = \frac{kr_c/D}{1 + kr_c/D}.$$

Note that κ is always less than 1. In particular, this model is estimated to be effective for a slow reaction after an encounter event [25]. Isoda *et al.* [26] proposed the so called "reactivity parameter" based on a similar concept. Their motivation is to explain the experimental data of the significantly reduced recombination rate for the electron-ion recombination [27,28] compared with the Langevin formula. The concepts presented in Refs. [24–26] look quite relevant in the present problem because the charges in the liquid dielectric are in the reverse-micelle form and it takes time for the surfactant molecules surrounding the micelles to be peeled off for ion neutralization. The effect of the external electric field can also produce the reduced recombination constant as shown in Refs. [26,29]. Unfortunately however, no recent literature can be found, dealing with theoretical or experimental studies on the ion-ion recombination for the liquid dielectric.

Finally, let us discuss the experimental and numerical paper of Kim *et al.* [3] on the EHD flow past three circular cylindrical electrodes with diameters of 1 mm within a 2D channel of a depth of 7.3 mm for use as a pumping device. In their numerical simulation, the electric field is obtained by solving Eq. (9) coupled with Eq. (13) where the linearized Onsager function $F_O(b) = 1 + 2\gamma E$ is used for (13). The charge density obtained from (14) is then substituted into Eq. (1b) to yield the flow field. Thus, the DSL effect is not considered in their paper. It is remarkable that the pumping velocity (streamwise velocity averaged over the channel cross section), obtained numerically, agrees well with the experimental data, even though the effect of the DSLs is neglected. In order to investigate the effect of the DSL on the pumping velocity, 2D simulation is performed again with COMSOL with various values of κ for the same arrangement of cylinders as in Ref. [3]. The side cylinders are grounded, and the central cylinder is applied to 2 kV dc. Furthermore, we set $\sigma_0 = 4.33 \times 10^{-9}$ S/m, $\eta = 1.34 \times 10^{-3}$ Pa s, $\varepsilon_0 = 2$, $m = 1$, and $\hat{a} = 2.25$ nm. Without reduction in α (i.e., with $\kappa = 1$), the pumping velocity is given as 8.8 mm/s, whereas, it becomes 7.0 mm/s at $\kappa = 0.15$; when κ is lowered below this, the simulation becomes unstable. Thus, only a 20% decrease in the pumping velocity is expected, even though α is decreased significantly. Unfortunately, we cannot validate the numerical solutions because experimental data with dc voltages are not available. Since the three-cylinder-electrode geometry is much more complex than the present one, exploring the fundamental reason for such nonsensitive dependence of the pumping velocity on the recombination constant is also beyond the scope of this paper.

V. CONCLUSIONS

We performed two kinds of experiments and 2D as well as 1D numerical simulations in order to study the competitive role of the Onsager effects in the bulk and DSL in determining the EHD flow over a pair of coplanar electrodes. Through our conductivity experiment with a pair of parallel facing electrodes, we confirmed the validity of the Onsager theory

as well as the related constant. From the flow-visualization experiment and numerical simulation on the EHD flow over coplanar electrodes, we have demonstrated that the flow is dominated by the bulk charge at a 1 mm gap of the electrode spacing, but at the decreased gap of 0.2 mm, the DSL effect is dominant and the central flow direction is reversed. This implies that, as the geometric scale is decreased, the DSL effect is more important than the bulk. In order to match the experimentally observed flow pattern as well as the measured fluid velocity, in our simulation, we reduced the recombination constant considerably from the Langevin theory. Fortunately, this adjustment does not affect the ionic size or the zero-field concentration, neither of which are allowed to vary arbitrarily because they are to be measured separately. Thus, a decrease in the recombination constant does not affect the creation of charge in the bulk, but it produces an increased slip velocity at the edge of the DSL through an increase in the wall electric field as well as the increased DSL thickness. The asymmetry in the flow pattern observed in the flow-visualization experiment can be reproduced with a 2D simulation by assigning different mobilities to each ion. We have also managed to find evidence of the reduction in the recombination constant from the experimental data of Gäfvert *et al.* [22]. Their distribution of the electric field within the space between a pair of parallel facing electrodes could be reproduced successfully by our 1D simulation with the recombination constant reduced to 0.065 times the values in the Langevin formula.

In the present paper, we confined ourselves to one kind of dielectric liquid, i.e., dodecane mixed with Span 80 in a 0.5 wt % fraction. Studies on other kinds of liquids with different concentrations are, of course, needed to make our conclusions more concrete. Although the rectangular domain used in this paper is very simple, we cannot avoid, in our theoretical or numerical papers, the unexplored mathematical singularity at the electrode edges. Extension to the EHD flow around electrodes with smoother geometry, such as circular electrodes, will also be interesting.

ACKNOWLEDGMENTS

This work was supported by the Human Resources Development of the Korea Institute of Energy Technology Evaluation and Planning (KETEP) grant funded by the Korea Government Ministry of Knowledge Economy (Grant No. 20114030200030). We thank Professor J. Carrier for reading the paper and D. S. Jo for his assistance with the conductivity measurement.

[1] Y. K. Suh, IEEE Trans. Dielectr. Electr. Insul. **19**, 831 (2012).
[2] J. C. Ryu, H. J. Park, and K. H. Kang, Phys. Rev. Lett. **104**, 104502 (2010).
[3] W. Kim, J. C. Ryu, Y. K. Suh, and K. H. Kang, Appl. Phys. Lett. **99**, 224102 (2011).
[4] A. I. Zhakin, in *Electrohydrodynamics*, edited by A. Castellanos (Springer, Wien/New York, 1998), Chap. 5.
[5] M. F. Hsu, E. R. Dufresne, and D. A. Weitz, Langmuir **21**, 4881 (2005).
[6] G. S. Roberts, R. Sanchez, R. Kemp, T. Wood, and P. Bartlett, Langmuir **24**, 6530 (2008).
[7] R. Kemp, R. Sanchez, K. J. Mutch, and P. Bartlett, Langmuir **26**, 6967 (2010).
[8] I. Abou-Nemeh and H. J. Bart, Langmuir **14**, 4451 (1998).
[9] Q. Guo, V. Singh, and S. H. Behrens, Langmuir **26**, 3203 (2010).
[10] A. S. Dukhin and P. J. Goetz, J. Electroanal. Chem. **588**, 44 (2006).
[11] J. K. Park, J. C. Ryu, W. K. Kim, and K. H. Kang, J. Phys. Chem. B **113**, 12271 (2009).
[12] Z. Randriamalala, A. Denat, J. P. Gosse, and B. Gosse, IEEE Trans. Electr. Insul. **EI-20**, 167 (1985).
[13] N. G. Green, A. Ramos, A. González, H. Morgan, and A. Castellanos, Phys. Rev. E **66**, 026305 (2002).
[14] Y. K. Suh and S. Kang, Phys. Rev. E **77**, 031504 (2008).
[15] Y. K. Suh and S. Kang, Phys. Rev. E **79**, 046309 (2009).
[16] B. D. Storey, L. R. Edwards, M. S. Kilic, and M. Z. Bazant, Phys. Rev. E **77**, 036317 (2008).
[17] M. Z. Bazant and T. M. Squires, Curr. Opin. Colloid Interf. Sci. **15**, 203 (2010).
[18] H. Zhao and H. H. Bau, Phys. Rev. E **75**, 066217 (2007).
[19] A. J. Pascall and T. M. Squires, Phys. Rev. Lett. **104**, 088301 (2010).
[20] A. Alj, A. Denat, J. P. Gosse, B. Gosse, and I. Nakamura, IEEE Trans. Electr. Insul. **EI-20**, 221 (1985).
[21] F. Nauwelaers, L. Hellemans, and A. Persoons, J. Phys. Chem. **80**, 767 (1976).
[22] U. Gäfvert, A. Jaksts, C. Törnkvist, and L. Walfridsson, IEEE Trans. Electr. Insul. **27**, 647 (1992).
[23] P. Debye, J. Electrochem. Soc. **82**, 265 (1942).
[24] F. C. Collins and G. E. Kimball, J. Colloid Sci. **4**, 425 (1949).
[25] S. A. Rice, P. R. Butler, M. J. Pilling, and J. K. Baird, J. Chem. Phys. **70**, 4001 (1979).
[26] K. Isoda, N. Kouchi, Y. Hatano, and M. Tachiya, J. Chem. Phys. **100**, 5874 (1994).
[27] Y. Nakamura, K. Shinsaka, and Y. Hatano, J. Chem. Phys. **78**, 5820 (1983).
[28] K. Shinsaka, M. Codama, T. Srithanratana, M. Yamamoto, and Y. Hatano, J. Chem. Phys. **88**, 7529 (1988).
[29] M. Obarowska and J. Godlewski, Synth. Met. **109**, 219 (2000).